

Tomographic imaging of transparent biological samples using the pyramid phase microscope

IGNACIO IGLESIAS*

Departamento de Física, Universidad de Murcia, Campus de Espinardo, 30100 Murcia, Spain

**iic@um.es*

Abstract: We show how a pyramid phase microscope can be used to obtain tomographic information of the spatial variation of refractive index in biological samples using the Radon transform. A method that uses the information provided by the phase microscope for axial and lateral repositioning of the sample when it rotates is also described. Its application to the reconstruction of mouse embryos in the blastocyst stage is demonstrated.

©2016 Optical Society of America

OCIS codes: (170.6900) Three-dimensional microscopy; (350.5030) Phase; (170.6960) Tomography.

References and links

1. J. Sharpe, U. Ahlgren, P. Perry, B. Hill, A. Ross, J. Hecksher-Sørensen, R. Baldock, and D. Davidson, "Optical projection tomography as a tool for 3D microscopy and gene expression studies," *Science* **296**(5567), 541–545 (2002).
2. J. Huisken, J. Swoger, F. Del Bene, J. Wittbrodt, and E. H. K. Stelzer, "Optical sectioning deep inside live embryos by selective plane illumination microscopy," *Science* **305**(5686), 1007–1009 (2004).
3. S. H. Ku, M. Lee, and C. B. Park, "Carbon-based nanomaterials for tissue engineering," *Adv. Healthc. Mater.* **2**(2), 244–260 (2013).
4. G. Popescu, *Quantitative Phase Imaging of Cells and Tissues* (McGraw-Hill, 2011).
5. I. Iglesias, "Pyramid phase microscopy," *Opt. Lett.* **36**(18), 3636–3638 (2011).
6. I. Iglesias and F. Vargas-Martin, "Quantitative phase microscopy of transparent samples using a liquid crystal display," *J. Biomed. Opt.* **18**(2), 026015 (2013).
7. I. Iglesias, "The quad-cell gradient sensor for the quantitative determination of the phase in microscopy," in *Digital Holography & 3-D Imaging Meeting* (Optical Society of America, 2015), p. DTh2A.1.
8. S. S. Kou, L. Waller, G. Barbastathis, and C. J. R. Sheppard, "Transport-of-intensity approach to differential interference contrast (TI-DIC) microscopy for quantitative phase imaging," *Opt. Lett.* **35**(3), 447–449 (2010).
9. W. Choi, C. Fang-Yen, K. Badizadegan, S. Oh, N. Lue, R. R. Dasari, and M. S. Feld, "Tomographic phase microscopy," *Nat. Methods* **4**(9), 717–719 (2007).
10. Y. Sung, W. Choi, N. Lue, R. R. Dasari, and Z. Yaqoob, "Stain-free quantification of chromosomes in live cells using regularized tomographic phase microscopy," *PLoS One* **7**(11), e49502 (2012).
11. K. Kim, Z. Yaqoob, K. Lee, J. W. Kang, Y. Choi, P. Hosseini, P. T. C. So, and Y. Park, "Diffraction optical tomography using a quantitative phase imaging unit," *Opt. Lett.* **39**(24), 6935–6938 (2014).
12. S. O. Isikman, W. Bishara, S. Mavandadi, F. W. Yu, S. Feng, R. Lau, and A. Ozcan, "Lens-free optical tomographic microscope with a large imaging volume on a chip," *Proc. Natl. Acad. Sci. U.S.A.* **108**(18), 7296–7301 (2011).
13. T. Kim, R. Zhou, M. Mir, S. D. Babacan, P. S. Carney, L. L. Goddard, and G. Popescu, "White-light diffraction tomography of unlabelled live cells," *Nat. Photonics* **8**(3), 256–263 (2014).
14. U. S. Kamilov, I. N. Papadopoulos, M. H. Shoreh, A. Goy, C. Vonesch, M. Unser, and D. Psaltis, "Learning approach to optical tomography," *Optica* **2**(6), 517–522 (2015).
15. T. Nguyen, G. Nehmetallah, D. Tran, A. Darudi, and P. Soltani, "Fully automated, high speed, tomographic phase object reconstruction using the transport of intensity equation in transmission and reflection configurations," *Appl. Opt.* **54**(35), 10443–10453 (2015).
16. M. T. Rinehart, H. S. Park, and A. Wax, "Influence of defocus on quantitative analysis of microscopic objects and individual cells with digital holography," *Biomed. Opt. Express* **6**(6), 2067–2075 (2015).
17. A. C. Kak and M. Slaney, *Principles of Computerized Tomographic Imaging* (IEEE Press, 1999).
18. K. Kim, H. Yoon, M. Diez-Silva, M. Dao, R. R. Dasari, and Y. Park, "High-resolution three-dimensional imaging of red blood cells parasitized by *Plasmodium falciparum* and in situ hemozoin crystals using optical diffraction tomography," *J. Biomed. Opt.* **19**(1), 011005 (2013).

1. Introduction

In recent years, numerous results have appeared describing the tomographic reconstruction of fluorescent markers in small biological samples or whole organisms, offering invaluable information on gene expression localization and the spatial distributions of molecules. At the

microscopic scale, optical projection tomography [1] and selective plane illumination microscopy [2] have proved to be very successful techniques for this purpose.

Relatively, less effort has been devoted to determining the three-dimensional morphology of unmarked tissues at microscopic scale, although such information may also be crucial to our understanding of processes involved in the developing organism or, as has emerged recently, in the engineering of functioning tissues from stem cells using, for example, carbon based nanomaterials as scaffolds to drive cell growth and differentiation [3].

In small transparent samples, the spatial distribution of different tissues is correlated with variability in optical density, i.e., with the distribution of the refraction index. One direct way of measuring this quantity is through the phase that the light acquires in a transillumination setup.

Different methods have been proposed to quantitatively measure the phase in biological samples [4]. We have shown that the pyramid phase microscope [5,6] or, in a more general sense, given that a glass pyramid is not fundamental for the method, the quad-cell [7] microscope, can provide reliable optical density data without using interference and its associated drawbacks by measuring the imbalance in the intensity that the wavefront generates on images acquired through a focal-plane split beam. Instead of other non-interferometric methods, such as those based on the transport of intensity equation, which measures the laplacian of the wavefront [8], the quad-cell microscope provides high density data of the gradient –a more direct function– of the wavefront with a very simple optical setup.

However, independently of the method used, transillumination phase maps represent – neglecting diffraction effects– the integrated phase, i.e., the sum of the different retardations that the tissue induces in the light path, not the three-dimensional distribution of optical density. This problem has been considered before and reconstruction algorithms have been developed and applied to the phase data obtained with a variety of techniques: interferograms registered for different illumination angles [9–11], lens-free holograms acquired from a multiplicity of angles [12], diffraction images obtained by focus scanning [13], training a neural network to infer the three-dimensional index distribution [14] or rotating the object, estimating the phase by the transport of intensity equation [15].

In this context, the aim of this paper is to show that the phase maps obtained by a quad-cell quantitative microscope –in this case implemented using a glass pyramid– can serve to obtain a tomographic reconstruction of the optical density of biological samples. Advantages of the technique compared with other techniques, mainly regarding the simplicity of the optical system and data processing, are discussed.

The paper is organized as follows: in the first part, the optical system and the phase gradient calibration procedure is described. The second part presents the mechanical system developed to hold and rotate the samples. Since defocus can impair the phase measurements [16], the third part presents a procedure to maintain the samples in focus during rotation and explains how the rotation axis is chosen. Experimental results of the reconstruction of mouse embryos are shown in the fourth section. Section five is dedicated to the conclusions.

2. Optical system and calibration

The optical part of the system is depicted in Fig. 1. A red LED (Oscon, Osram) with a 625 nm central wavelength, S, is used as source. To modulate the sensor [5], the light is passed through a static diffuser and, to control the dynamic range, through a diaphragm. Both components are stacked together and labeled jointly as D. After this, the light is collected by the lens L1 and an afocal system composed of lenses L2 and L3. The emerging light illuminates the sample which is placed inside a fused quartz cuvette, C, (Thorlabs) filled with water. Details of the sample holder and the rotation system are described later. The next part is a conventional optical microscope that uses a 20X microscope objective (Nikon, CFI PF ELWD 20X NA 0.45), labeled as MO in the figure, and the tube lens, TL. The microscope, images the sample onto a square aperture, SA, placed at the front focal plane of lens L4. A

glass pyramid, P, is placed at the back focal plane of L4 and an additional lens, L5, is used to image the sample onto a 1040x1392 pixels CCD camera, (1500M-CL-TE, Thorlabs).

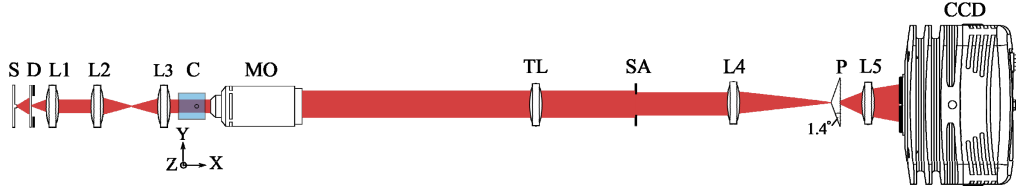


Fig. 1. Main optical system. S, a LED source; D, diffuser with circular diaphragm stacked together; L1-L5, lenses; C, glass cuvette; MO, microscope objective; TL, tube lens; SA, square aperture; P, glass pyramid; CCD, scientific grade camera.

To calibrate the system, a polystyrene bead (Polybead, Polysciences) with a refractive index of $n_F^s = 1.60$ and $90 \mu\text{m}$ in diameter was transferred from water to a planar receptacle made with a microscope slide and glued cover slips which was placed vertical in the front focal plane of the microscope objective. The receptacle was previously filled with index matching oil $n_F^h = 1.56$ (Cargille Labs) to simulate the index change of a biological sample in water. Given that the density of polystyrene and of the immersion medium is similar, the sphere remains static. When illuminated with a plane wave, it can be considered that the sphere generates a wavefront containing all the possible gradient variations from zero to infinity, and so serves to fully analyze the microscope response.

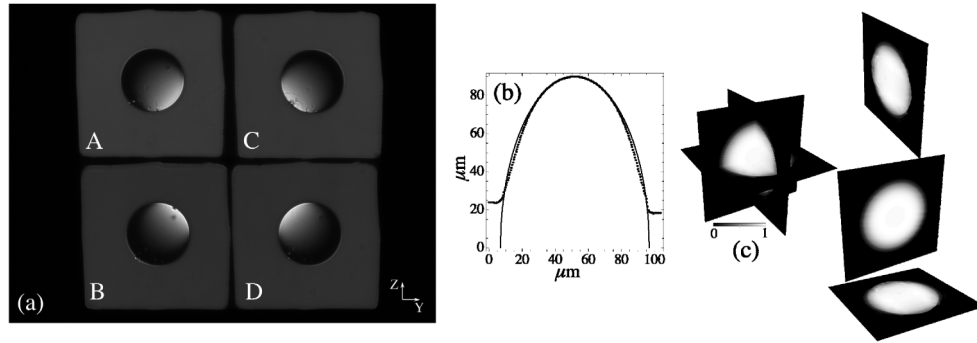


Fig. 2. System calibration and reconstruction. (a) An example of the acquired raw images of a polystyrene sphere of $90 \mu\text{m}$ in diameter; 1 px corresponds to $0.45 \mu\text{m}$. (b) Horizontal section (dotted line) of the integrated wavefront computed from the measured gradients and the theoretically expected wavefront (solid line). (c) Sphere reconstruction using the inverse Radon transform; the optical density has been normalized and is represented using the accompanying grayscale.

Figure 2(a), shows an example of the raw images that the camera acquires. Using a reference image (without the sample) and the information provided by the irregular shape of the mask, (SA in Fig. 1) as fiducial, the central coordinates of the subimages are computed and stored for subsequent division of the sample images to extract the four quadrant subimages (labeled A to D). The response to the input gradient is obtained using the expressions [5]

$$\begin{aligned} s_y &= ((C+D)-(A+B))/((A+B+C+D)) \\ s_z &= ((B+D)-(A+C))/((A+B+C+D)) \end{aligned} \quad (1)$$

where **A**, **B**, **C** and **D** matrices represent the subimages and the division an element-wise operation. The response in the orthogonal directions given by s_y and s_z is corrected according to the expected phase slope that a sphere with the same radius will generate to

obtain two new phase gradient matrices \mathbf{g}_y and \mathbf{g}_z . The system range—the maximum slope before the system becomes saturated—is determined by the diameter of the illumination diaphragm after the diffuser. From the two gradient images the phase map is obtained using for integration a least-squared error-minimization algorithm to solve the Poisson's equation. Figure 2(b) shows the results of the integration for a normal plane, where the wavefront is represented scaled to the microsphere radius. The effect on the integration of the sensor saturation can be seen: for the particular diaphragm radius used in the current system, saturation occurs approximately at a slope of $\tan \theta = 1.4$; for higher slopes, the measured gradient takes its maximum value and remains constant. Comparing the computed values (dotted line) with the expected curve (solid line) it can be appreciated that the algorithm slightly underestimates the phase for high gradients. In addition, the experimental curve shows a slight asymmetry caused by a small global tilt in the wavefront.

Under the assumption that the obtained phase map is generated by the sum of the phase delays that the light suffers when traversing the sample, the three dimensional index distribution of the object can be recovered using the Radon [17] transform utilizing phase maps for different angles as projections.

To check the capability of the system to reconstruct the polystyrene sphere of uniform index, we considered that all the projections would be equal if the rotation axis perfectly coincides with the sphere symmetry axis. Assuming this, the inverse Radon transform (using a Hann filter and cubic interpolation) were used with a unique phase map reassigned to simulate acquisition during a 360° sphere rotation. Figure 2(c) shows the reconstruction of the optical density. The underestimation of the integrated phase for high gradient values emerges, as the exploded view shows, as a slightly smaller than expected refraction index, close to the sphere surface.

We considered these results to be good enough to attempt applying the method to biological samples.

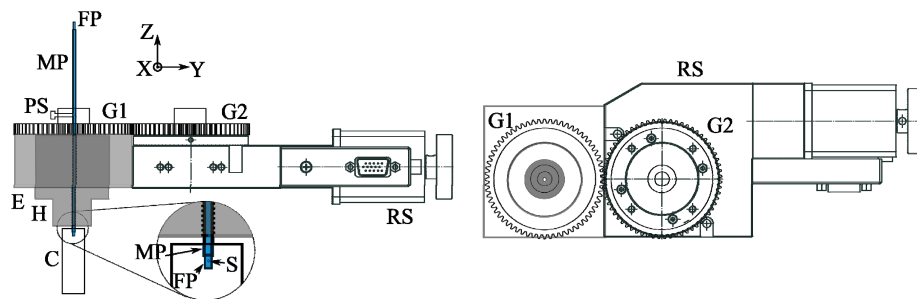


Fig. 3. The rotation system, where FP is the FEP tube filled with agarose; MP, is the glass micropipette; PS, is a plastic screw; G1 and G2, are gears; RS is the rotation stage; E, an extension of the rotation stage platform; H, the micropipette holding piece; C, water cuvette. The inset shows an augmented view of the system showing the position of the sample, S.

3. Sample holding and rotation

To rotate the samples the following system was used. A fluorinated ethylene propylene (FEP) tube (Adtech) of 0.3 mm inner diameter and 0.5 outer diameter was inserted in a glass micropipette (Intramark black, Brand) of 0.5 mm inner diameter and 1.3 mm outer diameter, which acted as spinner. One of the extremes of the FEP tube was connected to a micro-syringe. The sample was transferred to melted low-gelling-temperature agarose (Sigma) and then suctioned to the FEP tube using the micro-syringe where it was left to cool and become immobilized.

As Fig. 3 shows, the micropipette, MP, with the FEP tube (containing the sample immersed in solidified agarose), FT, inside, is inserted in a plastic holder, H, attached to the rotation stage platform, RS, (DT-80, Micos). This part was carefully drilled so that the glass micropipette needed slight pressure when being displaced to be immersed in the water

cuvette, C. Once the position of the glass micropipette is established –close to, but out of the field of view– it is locked with a plastic screw, PS, to move solidary with the rotation gear G1, which is moved by a second gear, G2, fixed to the rotation stage. This setup translates the rotation movement of the gear to the micropipette which then rotates around its axis of symmetry, transmitting the movement to the FEP tube. The final step in preparing the sample for imaging is to move the FEP tube up and down inside the glass micropipette to center the sample, labeled as S in the enlarged view of the inset in Fig. 3, in the microscope field of view. Given the similar values of the refractive index of the FEP, agarose and water, and the square geometry of the cuvette, only the sample –if the FEP tube wall is out of the field of view– generates a significant local phase variation in the measured light.

4. Correcting the rotation drift

The above described system minimizes the drift of the glass micropipette i.e. the unwanted lateral and axial displacement of the micropipette depending on the rotation angle. The drift that remains is caused by limited glass straightness along the last section: between the holder (H in Fig. 3) and the cuvette (C in Fig. 3). Besides, an additional drift is added to the specimen since the section of the FEP tube protruding from the glass micropipette and submerged in water (see the inset in the Fig. 3) is always slightly bent. The first deleterious effect of this drift is that the rotation axis of the FEP-agarose tube ends up far from the symmetry axis of the sample, impacting on the quality of the tomographic reconstruction. Also, the axial component of the drift becomes critical with the 20x objective due to the limited focus depth of the microscope.

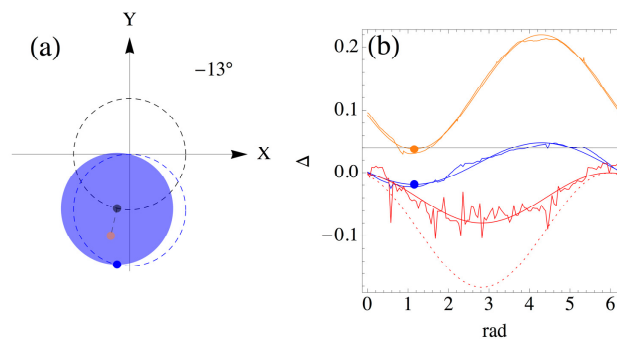


Fig. 4. (a). Modeling of the eccentric rotation of a section of the agarose column (light blue disk) containing the sample. Light propagates along the X direction. The dark blue point marks the left border (looking at the light) of the agarose disc interfacing with the FEP tube wall (not shown). The blue dashed circle represents the trajectory of this border, the black point represents the center of the agarose disk, whereas the black dashed circle its trajectory when the motor rotates; the orange dot is a point close to the specimen location. (b) Focusing curves representing displacements, Δ , versus the angle. In orange, the sample mass center lateral displacement, in blue and red, the lateral and axial displacement of the interface agarose-FEP. The dashed red curve represents the computed axial correction of the sample position. A displacement of 0.01 units represent $10.2 \mu\text{m}$.

Figure 4(a) shows the modeling of the problem depicting a section of the agarose column (disc in light blue), which, instead of rotating (figure depicts a 13° counterclockwise rotation angle) around its symmetry center (labeled as a black dot), this point follows the orbit depicted as a dashed circle in black.

To counteract this unwanted movement, the rotation system of Fig. 3 is mounted on top of two linear translation stages (PLS-85, Micos) (not shown in the figure) to move the sample along the optical axis (X-axis) and along the lateral axis (Y-axis).

To determine the movements of the linear translation stages for each angle, one complete rotation is first executed. In this rotation, the location of the FEP tube is determined using the phase jump that occurs between the tube internal surface and the agarose (blue point in the

scheme of Fig. 4(a)), which provides a clear signal to carry out a focus search procedure. The signal is obtained using the A-C quadrants (see Fig. 1(a)) to measure the gradient only in the lateral direction (Y-axis). The derivative of the average along the row dimension produces a sharp minimum when the FEP-agarose interface is in focus. Using this signal, a Golden section search algorithm is executed for each rotation angle by moving the axial translation stage. When the minimum is reached, the corresponding pixel determines the lateral coordinate of the interface. Figure 4(b) shows the results obtained for a particular experiment. The curves in blue correspond to the measured lateral coordinates and its Levenberg-Marquardt fit to a cosine model function, while the curve in red corresponds to the focal position measurements. The blue dot in Fig. 4(b) indicates the minimum of the lateral coordinate and its angular coordinate the phase shift with respect to the origin of angles of the rotation stage.

The position of a sample embedded in the agarose column (depicted in the scheme of Fig. 4(a) as an orange dot) follows the same curve as the interface but with a possible angular shift and different amplitude. To determine both parameters, an additional complete rotation is carried out tracking the lateral Y-coordinate of the sample mass center using the intensity (sum of the four quadrants subimages) for each angle. Given the object transparency, the tracked mass center is computed from the distribution of the minimum values using a threshold. These values are mainly associated with the sample interface with the agarose. Figure 4(b) shows in orange, an example of the mass center tracking. Even though these values cannot be used directly to correct the rotation axis since they depend on the sample intensity image for each angle, the fit to a cosine can, since it describes the movement of a point close to an approximate symmetry axis of the sample minimizing interpolation in the Radon inverse transform. In the particular case depicted in Fig. 4(b), the shift between the border lateral position and the sample mass center lateral position—the difference between the angular coordinates of the blue and orange points in the Fig. 4(b)—is small, close to the situation depicted in the scheme of Fig. 4(a).

The information needed to bring the sample into focus (dotted curve in red in Fig. 4(b)) is obtained from the fitted curve of the border axial position (solid red curve in Fig. 4(b)) after scaling in accordance with the amplitude of the lateral displacement and shifted by the difference between the angular positions of the blue and orange points of Fig. 4(b).

It should be noted that the sample itself cannot be used to determine the focus position due to the difficulties in establishing a focal condition for a generic object and that this procedure generates data to bring the sample to the focus plane independently of its position in the agarose column.

The developed software carries out two complete rotations but the operations for each angle can be merged into one to speed up the process.

5. Tomographic reconstruction of mouse embryos

The algorithm was applied to the reconstruction of fixed mouse embryos at a development stage of about four days. The samples were mounted as described above using agarose at 1.5 w/v(%). Figure 5(a), shows the normalized reconstructed phase for the 0° projection, taking as zero the phase induced by the agarose immersion medium. The phase map shows a spheroid with a complex structure emerging from the superior pole, features that correspond to a hatching blastocyst. Cell accumulation must be responsible of the high values of optical density that can be seen close to the hatching pole.

1800 images were registered during a 360° sample rotation ([Visualization 1](#) shows a video of the full set). Whereas the exposure time per image was 11 msec, one second was spent at each angle before acquisition to ensure fading of the mechanical vibrations induced by the movements of the motors. Figure 5(b) shows the result of the Radon reconstruction, where, after normalization of the obtained data, only one band of optical density between 0.25 and 0.30 is represented; the color map is extended to smaller values to improve visualization over the black background. [Visualization 2](#), shows a 360° rotation of Fig. 5(b). Figure 5(c), shows the normalized optical density map for a central frontal plane. From the above figures, it is

apparent that the main spheroidal structure of the blastocyst accumulates embryonic endoderm cells close to the surface but not evenly given that an area appears in the surface with an optical density close to the value of the surrounding agarose. Also, the hatching part contains a complex structure with smaller spheroidal structures, which also accumulate cells, mainly at the surface.

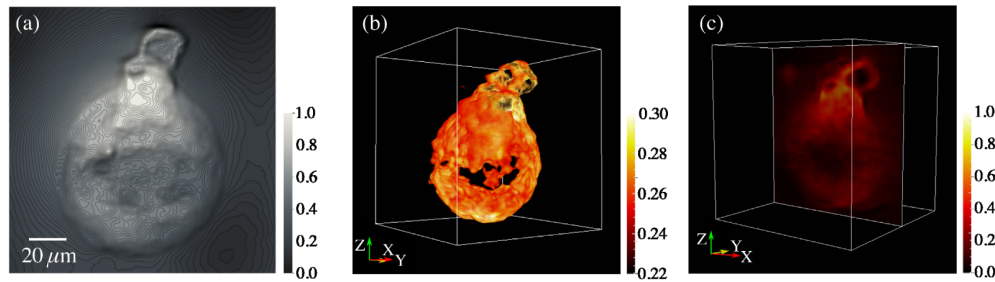


Fig. 5. (a) Image (315x315px) showing the phase topographic map for a particular angle ([Visualization 1](#) shows the complete set); the white bar represents 20 μm ; the gray scale assigns 0 to the agarose background and 1 to the maximum optical density in the field. (b) Three-dimensional representation of an optical density band of the Radon reconstruction (see [Visualization 2](#) to observe the figure rotation). (c) Optical density map in a frontal plane. The outlines in (b) and (c) mark the limits of a volume of 128.2x128.2x137.2 μm .

6. Conclusions

We have shown that the pyramid phase microscope can be applied to the three-dimensional reconstruction of optical density variations in biological samples.

The method proposed to reposition the sample allows the focus to be maintained and to define a rotation axis that alleviates interpolation independently of the sample location in the holding medium. Consequently, it permits the use of water immersion objectives of higher magnification to study smaller samples without changing the mechanics or the sample mounting method the only limitation being the working distance, which must be sufficient to accommodate the FEP tube.

The use of the mass center of the whole specimen is just one possibility, but the same strategy can be applied to a region of interest to track specific features, by establishing an adapted rotation axis that will improve the tomographic reconstruction of specific sub-volumes by reducing interpolation.

The experimental results shown correspond to a fixed specimen but there are no limitations for the applicability of the proposed system to biological samples *in vivo*, adapting the sample immersion medium to physiological conditions. Furthermore, a lateral excitation laser beam (as in SPIM) can be easily added to the system to carry out simultaneous fluorescence tomography experiments.

The camera used did not have sufficient high resolution to reconstruct detailed phase variations. With the current system only phase maps of around 490x490 pixels could be obtained. However, this can be solved with a better camera or using an electrooptical device to sequentially block the quadrants instead of a glass pyramid [6] to acquire the required subimages using the complete CCD sensor.

Finally, a diffraction tomography algorithm [18] might be considered instead of the projection algorithm in order to improve the results by taking into account the diffraction effects in the phase images.

Acknowledgments

The author thanks Joaquín Gadea of the Departamento de Fisiología of the Universidad de Murcia for help in the preparation of the biological samples and Alfonso Gutierrez-Adan from the Instituto Nacional de Investigación y Tecnología Agraria y Alimentaria, Madrid for providing the samples.